PHYSICAL REVIEW B **101**, 024302 (2020)

Local structure and atomic dynamics in Fe_2VAl Heusler-type thermoelectric material: The effect of heavy element doping

K. Kimura,[1,*] K. Yamamoto,[1] K. Hayashi,[1,2] S. Tsutsui,[3] N. Happo,[4] S. Yamazoe,[5] H. Miyazaki,[1] S. Nakagami,[1]
J. R. Stellhorn,[6,†] S. Hosokawa,[6] T. Matsushita,[3,‡] H. Tajiri,[3] A. K. R. Ang,[1] and Y. Nishino[1]
[1]*Department of Physical Science and Engineering, Nagoya Institute of Technology, Nagoya 466-8555, Japan*
[2]*Frontier Research Institute for Materials Science, Nagoya Institute of Technology, Nagoya 466-8555, Japan*
[3]*Japan Synchrotron Radiation Research Institute (JASRI), SPring-8, 1-1-1 Kouto, Sayo, Hyogo 679-5198, Japan*
[4]*Department of Computer and Network Engineering, Hiroshima City University, Hiroshima 731-3194, Japan*
[5]*Department of Chemistry, Graduate School of Science, Tokyo Metropolitan University, Tokyo 192-0397, Japan*
[6]*Department of Physics, Kumamoto University, Kumamoto 860-8555, Japan*

(Received 7 April 2019; revised manuscript received 17 November 2019; published 7 January 2020)

X-ray absorption fine structure (XAFS), x-ray fluorescence holography (XFH), and inelastic x-ray scattering (IXS) techniques were applied to an $Fe_2(V_{0.95}Ta_{0.05})Al$ Heusler-type thermoelectric material to investigate the doping effect of Ta on the local structure and the atomic dynamics. The XAFS and XFH results show that the positional correlation between Ta and surrounding Fe atoms is much more rigid than that between V and Fe. In the IXS results, we observed a broad dispersionless mode in the energy range of the acoustic phonons of undoped Fe_2VAl, which is regarded as the so-called resonant mode. These results revealed a clearly different feature of the dynamics of heavy dopants from that of the matrix element, which disturbs the coherency of phonons and should contribute to the enhancement of the thermal insulation.

DOI: 10.1103/PhysRevB.101.024302

I. INTRODUCTION

Element doping is a broadly adopted strategy for enhancing the performance of thermoelectric materials. The performance of thermoelectric materials is expressed by the dimensionless figure of merit, $ZT = (S^2/\rho\kappa)T$, where T is temperature, S is the Seebeck coefficient, ρ is electrical resistivity, and κ is thermal conductivity. Thus, a low κ value is highly desirable to achieve high ZT. The thermal conductivity is the sum of the electronic and lattice components, that is, $\kappa = \kappa_e + \kappa_{ph}$. Since κ_{ph} is independent of S and ρ, unlike κ_e, which is empirically proportional to the electrical conductivity, suppression of κ_{ph} can efficiently increase the ZT value. In most cases, the value of the lattice thermal conductivity κ_{ph} can be substantially reduced by doping an element.

So far, several mechanisms have been proposed to explain the κ_{ph} reduction induced by doping. Traditionally, κ_{ph} reduction has been explained in terms of the perturbation theory constructed by Klemens, Ziman, and Callaway [1–3]. This approach treats the scattering of phonons by static imperfections and has provided the foundation to describe the κ_{ph} reduction observed in various thermoelectric materials such as Si-doped Mg_2Sn [4], Se-doped PbTe [5], and half-Heusler alloys [6]. On the other hand, the importance of the dynamic properties of dopants has been pointed out, especially in the case of cage compounds, such as skutterudites [7] and clathrates [8], in which the rattling of guest atoms in cages is considered to suppress κ_{ph}. Furthermore, a recent inelastic neutron scattering (INS) study [9] indicated that the dynamics of dopants is influential in κ_{ph} reduction even in the simpler systems, i.e., Ir- or Os-doped FeSi [10]. In this INS study, the so-called resonant mode of a dopant [11] was observed, which was discussed in relation to the suppression of κ_{ph}. Also, the importance of dopant dynamics was revealed for Si nanostructures using first-principles calculations of κ_{ph} [12].

The Fe_2VAl Heusler-type thermoelectric material [13] is a suitable candidate for investigating the effect of doping on κ_{ph}. This is because the Bravais lattice of Fe_2VAl is fcc with only four atoms in the unit cell (Fig. 1 [14]), which is remarkably simpler than the structure of other thermoelectric materials, such as Bi chalcogenides, skutterudites, and clathrate compounds [15]. Thus, a precise discussion about phonons will be possible to understand the doping effect on thermal insulation.

In previous studies for Fe_2VAl doped with Ge, Si, and W [16,17], the reduction in κ_{ph} was discussed based on the Klemens perturbation theory [1]. This theory qualitatively explains the tendency that heavier dopants more efficiently suppress κ_{ph}. However, atomic level information of the doping effect has not been adequately obtained, which would be necessary to elucidate the origin of κ_{ph} reduction and to refine the theory to predict the doping effect on thermal insulation. In particular, dynamic properties of dopants, which potentially affect κ_{ph}, have not been taken into account in this system.

---

[*] kimura.koji@nitech.ac.jp

[†] Present address: Applied Physics and Chemistry, Faculty of Engineering, Hiroshima University, Higashi-Hiroshima, Hiroshima 739-8527, Japan.

[‡] Present address: Graduate School of Materials Science and Technology, Nara Institute of Science and Technology, Ikoma, Nara, 630-0192, Japan.

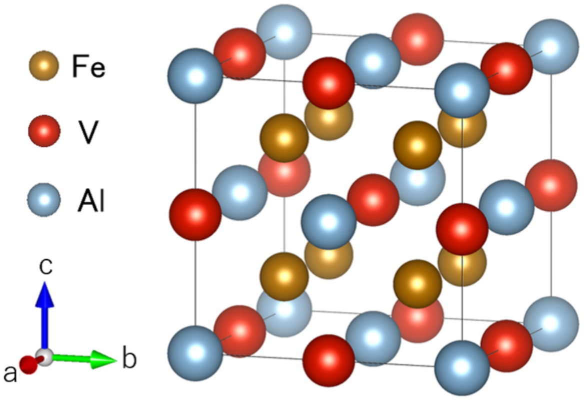

FIG. 1. Crystal structure of Fe_2VAl [14].

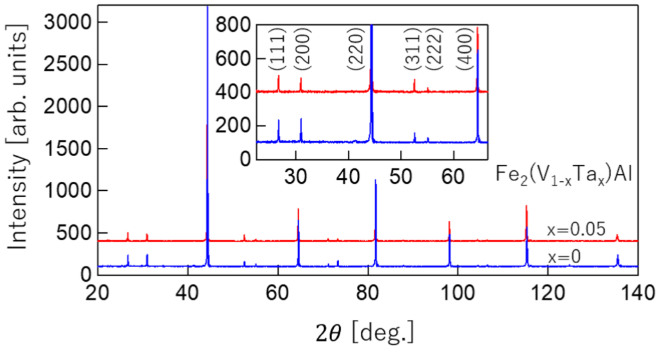

FIG. 2. XRD pattern of $Fe_2(V_{0.95}Ta_{0.05})Al$ and Fe_2VAl powders. Cu $K\alpha$ radiation was used as the incident x-ray.

X-ray absorption fine structure (XAFS) and x-ray fluorescence holography (XFH) measurements provide local structural information about dopants, which is useful to obtain microscopic understanding of the doping effect. These techniques are sensitive to thermal vibration of dopants, and thus, atomic level information of their dynamics can be investigated. XAFS is a widely used technique, which can evaluate the thermal vibration in the radial direction through the Debye-Waller factor or the rms displacement. On the other hand, XFH is a relatively new technique [18–20], which can visualize the three-dimensional atomic configurations around a specific element without assuming any structural models and has been applied to various materials [21–29]. The intensity and the shape of the obtained atomic image strongly reflect the positional fluctuations of the central or surrounding atoms [30–36], and thus, this technique is available to evaluate thermal vibrations of dopants. Although the spatial resolution of XFH is worse than XAFS, XFH has the advantage that it provides three-dimensional atomic images around the dopant within a wide range of about 1 nm.

Moreover, the doping effect on phonon dispersion relations is also of great importance to clarify the microscopic origin of the κ_{ph} reduction. Since phonons are the carrier of the heat, variation in the phonon dispersion caused by the doping should provide valuable insight into κ_{ph} reduction. Phonon dispersion relations can be investigated using inelastic x-ray scattering (IXS). So far, IXS techniques have been applied to several thermoelectric materials, such as PbTe [37], skutterudites [38–40], and sodium cobaltate [41], in order to understand low κ_{ph} values realized in these systems. On the other hand, the phonon dispersion of Fe_2VAl was investigated only theoretically using first-principles calculations [42–44]. Theoretical approaches are, of course, useful to obtain detailed information about phonons, such as the partial density of states (PDOS), but they are demanding for systems including dopants, where the translational symmetry of the crystal is not available. Therefore, an IXS experiment is indispensable to obtain phonon dispersions of Fe_2VAl containing dopants. Since the scattering strength for x-rays is approximately proportional to the square of the atomic number, IXS is sensitive to heavy elements and provides information complementary to INS. Therefore, IXS is suitable to detect variations in phonon dispersions caused by a small amount of heavy dopants, which, in general, suppress κ_{ph} more efficiently than light dopants.

In this study, XAFS, XFH, and IXS techniques are applied to $Fe_2(V_{0.95}Ta_{0.05})Al$, which exhibits a lower κ_{ph} value by about 45% compared with that of the undoped Fe_2VAl [45]. The XFH and XAFS experiments reveal much stronger positional correlations between Ta and surrounding Fe than between V and Fe. Also, we find a dispersionless vibrational mode of Ta in the IXS results which is considered the resonant mode of Ta. On the basis of these observations, dynamic properties of Ta and their effect on κ_{ph} are discussed.

II. EXPERIMENT AND ANALYSIS

Ingots of Fe_2VAl and $Fe_2(V_{0.95}Ta_{0.05})Al$ were prepared by repeating arc melting of 99.99% pure Fe and Al and 99.9% pure V and Ta in an argon atmosphere. The ingots were homogenized at 1273 K for 48 h in vacuum. Since single crystals are required for XFH and IXS measurements, they were grown from these ingots using the Czochralski method in a tri-arc furnace. Then, the crystals were cut along the (100) plane. The diameters and the thicknesses of the obtained samples are about 5 and 1 mm, respectively. Here, the crystal orientations were confirmed by the Laue method. The real compositions of undoped and Ta-doped samples were confirmed to be $Fe_{1.996}V_{1.061}Al_{0.943}$ and $Fe_{2.027}V_{0.970}Ta_{0.058}Al_{0.945}$, respectively, using energy dispersive x-ray spectroscopy with an electron microscope. For the XAFS measurements, powder samples of $Fe_2(V_{0.95}Ta_{0.05})Al$ and Fe_2VAl diluted with BN powder were prepared and were pressed into a pellet. The x-ray diffraction (XRD) measurements were performed for these powder samples as shown in Fig. 2. The x-ray wavelength was 1.54 Å (Cu $K\alpha$ radiation). The XRD patterns confirm the $L2_1$ Heusler-type structure of these samples [45]. The assigned indexes are indicated in the inset in the range of 2θ below 75°.

V K-edge (5.465 keV) and Ta L_{III}-edge (9.881 keV) XAFS measurements for $Fe_2(V_{0.95}Ta_{0.05})Al$ were performed at BL01B1 in the SPring-8. The V K-edge XAFS experiment for undoped Fe_2VAl was also carried out. The incident x-ray beam was monochromatized by a Si(111) double-crystal monochromator. The measurements were performed at room temperature. The V K-edge spectrum was measured in the transmission mode using two ionization chambers in front of

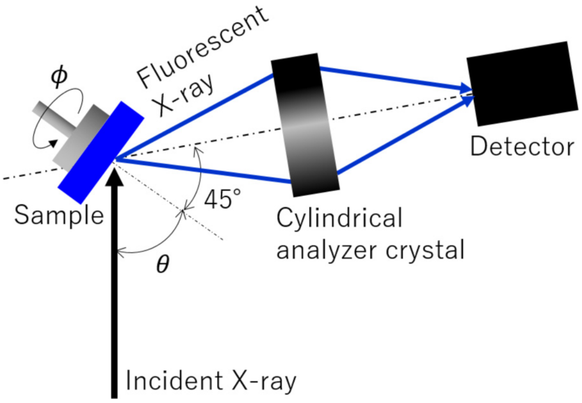

FIG. 3. Experimental geometry for the XFH measurements.

and behind the sample, which are filled with a mixture of helium and nitrogen gases and with nitrogen gas, respectively. The Ta L_{III}-edge spectrum was recorded in the fluorescence mode using an ion chamber and 19 solid-state detector as monitors of the incident beam and the fluorescent x-ray intensities, respectively. Here, the ionization chamber was filled with a mixture of nitrogen and argon gases. The ranges of the energy scans for V K-edge and Ta L_{III}-edge XAFS were from 5.4 to 6.4 keV and from 9.8 to 10.8 keV, respectively.

The extended XAFS (EXAFS) oscillations $\chi(k)$ were extracted from the raw absorption and fluorescence data using the REX 2000 software package provided by Rigaku Corporation. Then the Fourier transformation (FT) was applied to $k^3\chi(k)$, and the FT magnitude $|F(r)|$ was obtained. The neighboring area of $|F(r)|$ was inverse Fourier transformed to obtain $k^3\chi(k)$ concerning the corresponding neighboring atoms. The obtained $k^3\chi(k)$ was fitted by the theoretical formula

$$\chi(k) = S_0^2 \sum_i \frac{N_i}{kr_i^2} f_i(k,\pi)\sin[2kr_i + \phi_i(k)]e^{-2[\sigma_i^2k^2 + r_i/\lambda(k)]},$$

where S_0^2 is the amplitude reduction factor, N_i is the coordination number, r_i is the interatomic distance, $f_i(k,\pi)$ is the backscattering atomic form factor, σ_i is the rms displacement, $\phi_i(k)$ is the phase shift, and λ is the mean free path of photoelectrons. The index i is the label of the neighboring atoms. Among these parameters, $f_i(k,\pi)$, $\phi_i(k)$, and λ were evaluated using the FEFF8 program [46]. In this manner, the values of r_i and σ_i were obtained.

The XFH measurements were performed at BL13XU at the SPring-8 and BL6C at the Photon Factory in Japan. We measured Ta $L\alpha$ (8.15 keV) and V $K\alpha$ (4.95 keV) holograms of the $Fe_2(V_{0.95}Ta_{0.05}Al)$ single crystal using the incident x-ray energies from 11.9 to 14.4 keV in steps of 0.5 keV. The measurements were performed at room temperature. The incident beam intensity was monitored with an ionization chamber. The Ta $L\alpha$ and V $K\alpha$ fluorescent x-rays were analyzed and focused by a cylindrical graphite crystal and monitored by an avalanche photodiode and a silicon drift detector, respectively. The ranges of azimuthal ϕ and incident θ angles were $0^\circ \leqslant \phi \leqslant 360^\circ$ in steps of 0.25° and $0^\circ \leqslant \theta \leqslant 75^\circ$ in steps of 1°, respectively. These angles are illustrated in Fig. 3, which shows the geometry of the XFH experiment. Details of the experimental setup are described in Ref. [19]. The obtained holograms are corrected taking into account the suppression of the holographic oscillations caused by the beam attenuation effect [47]. The Barton algorithm was used for the reconstruction of atomic images [48].

IXS measurements were performed on Fe_2VAl and $Fe_2(V_{0.95}Ta_{0.05})Al$ at BL35XU in the SPring-8 [49]. The Si(11 11 11) backscattering setup was used. The energy resolution was about 1.5 meV at an incident energy of 21.747 keV. The q resolution was $\Delta\boldsymbol{q} = (0.05, 0.02, 0.05)$ in reciprocal lattice units of Fe_2VAl. The measurements were performed in the two Brillouin zones (BZs) having the (800) and (600) Γ points, which are suitable to detect the acoustic and optical phonons, respectively, because of the strong and weak Bragg peak intensities of the (800) and (600) reflections. In these BZs IXS from longitudinal and transverse phonons in the [100] direction was measured. The measurements were performed at room temperature.

III. RESULTS

Figure 4(a) shows the V K- and Ta L_{III}-edge EXAFS oscillations $k^3\chi(k)$ of $Fe_2(V_{0.95}Ta_{0.05})Al$. Here, $k^3\chi(k)$ of the V K-edge of undoped Fe_2VAl is also shown. The amplitude of the Ta L_{III}-edge oscillation is larger than those of the V K-edge oscillations of both $Fe_2(V_{0.95}Ta_{0.05})Al$ and Fe_2VAl, especially in the high-k region, suggesting different local environments between Ta and V.

The FT magnitudes $|F(r)|$ are shown in Fig. 4(b). The important feature observed in Fig. 4(b) is the larger height of the first peak for the Ta L_{III}-edge result than that for the V K-edge result, reflecting the larger amplitude of the Ta L_{III}-edge oscillation [Fig. 4(a)]. This peak may correspond to the first neighboring Fe atoms. Moreover, the peak at around $r = 2.65$ Å is observable for the Ta L_{III}-edge result, which may be attributed to the Ta-Al peak, whereas it is not clear for the V K-edge results for both Ta-doped and undoped samples.

Figure 4(c) shows the results of the curve fitting. The experimental curves are obtained by the inverse Fourier transformation of $|F(r)|$ in the ranges of $1.84 < r < 2.84$ Å for the Ta L_{III}-edge result and $1.80 < r < 2.88$ Å for the V K-edge results of both Ta-doped and undoped samples. These ranges include the first and second coordination shells. In the fitting procedure, Ta was placed at the V site according to the previous XRD results [45], which indicate that Ta enters the V site. The coordination numbers of the first and second shells were fixed to 8 and 6, corresponding to the surrounding Fe and Al atoms, respectively. As shown in Fig. 4(c), we can confirm that the fitting curve well reproduces the experimental results. The derived values of r_i and σ_i are summarized in Table I.

The obtained V-Fe and V-Al distances for the Ta-doped sample are not significantly different from those of the undoped one, which suggests that Ta doping does not strongly affect distances between V and the surrounding atoms. On the other hand, the Ta-Fe and Ta-Al distances are significantly larger than those around V, which is reasonable when considering the larger atomic radius of Ta compared to V.

The rms displacements are, overall, larger around V than those around Ta. This is consistent with the higher first and

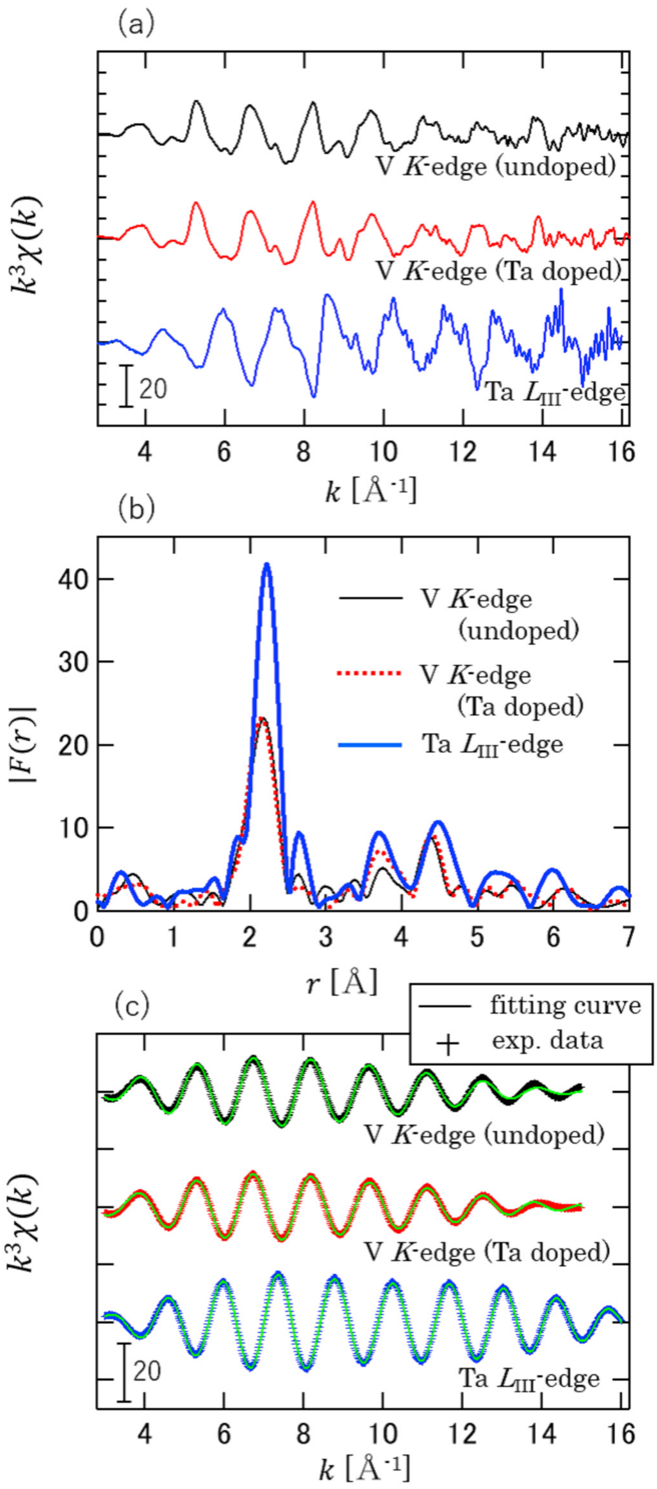

FIG. 4. (a) V K- and Ta L_{III}-edge EXAFS oscillations $k^3\chi(k)$ and (b) the corresponding Fourier transformed EXAFS spectra $|F(r)|$ of $Fe_2(V_{0.95}Ta_{0.05})Al$. The V K-edge results obtained from the undoped Fe_2VAl are also shown. (c) The $k^3\chi(k)$ curves obtained by the inverse Fourier transformation of $|F(r)|$. The results of the curve fitting are also shown with the solid lines.

TABLE I. The values of the interatomic distance r_i and the rms displacement σ_i obtained by the curve fitting shown in Fig. 4(c).

Atomic pair	r_i (Å)	σ_i (Å)
V-Fe (undoped)	2.479 ± 0.003	0.084 ± 0.004
V-Fe (Ta doped)	2.500 ± 0.007	0.090 ± 0.004
Ta-Fe	2.548 ± 0.009	0.06 ± 0.01
V-Al (undoped)	2.84 ± 0.06	(0.2)
V-Al (Ta doped)	2.83 ± 0.02	0.09 ± 0.09
Ta-Al	2.90 ± 0.04	0.06 ± 0.06

second peaks observed in the Ta L_{III}-edge results as shown in Fig. 4(b). The extremely large value of 0.2 Å in the undoped sample (denoted in the parentheses in Table I) is due to the difficulty in detecting the small V-Al peak at around 2.65 Å in Fig. 4(b) in the fitting procedure. Such a difficulty would also be reflected in the large errors for σ_i of V-Al and Ta-Al pairs in the Ta-doped sample.

The holograms of V $K\alpha$ and Ta $L\alpha$ lines are displayed in Figs. 5(a) and 5(b), respectively. These holograms are measured at an incident energy of 12.4 keV. Clear standing wave lines are observed, showing that the experiments were successfully performed.

The reconstructed atomic images of the Fe plane around V are shown in Fig. 6(a). Circles indicate the expected positions of Fe atoms around V derived from the crystal structure of Fe_2VAl. Clear atomic images are observable within the circles, especially at the positions of first- and second-nearest Fe. Figure 6(b) shows the corresponding atomic images around Ta. The positions of the spots agree well with those around V. On the other hand, the intensity of the atomic images is stronger around Ta than around V, which is consistent with the EXAFS results mentioned above. This behavior is in contrast to the observation that atomic images around dopants exhibit weaker intensity than those around matrix elements [30,35]. In addition, stronger intensities around Ta are observed in a wide spatial range of more than 10 Å. The images observed in the interstitial region, e.g., at about $(x, y) = (1.5, 5.5)$Å in Fig. 6(a), are considered to be artifacts, which could be caused by the limited number of holograms recorded with the different energies.

Figures 7(a)–7(d) show the IXS spectra of Fe_2VAl measured in the geometry to detect the longitudinal acoustic (LA), transverse acoustic (TA), longitudinal optical (LO), and transverse optical (TO) modes, respectively. Here, we select two BZs with the (800) and (600) Γ points, which are suitable to observe acoustic and optical phonons, taking into account that the intensity of the (800) Bragg reflection is about one order of magnitude stronger than that of the (600) Bragg reflection. Note that the intensities of long-wavelength

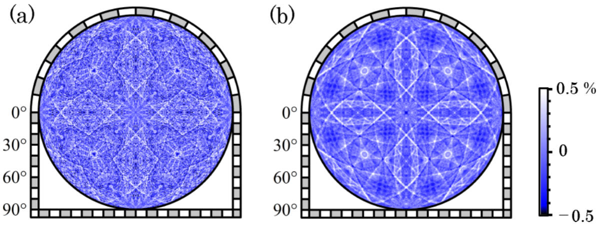

FIG. 5. (a) V $K\alpha$ and (b) Ta $L\alpha$ holograms obtained at an incident energy of 12.4 keV, measured with a silicon drift detector and avalanche photodiode, respectively.

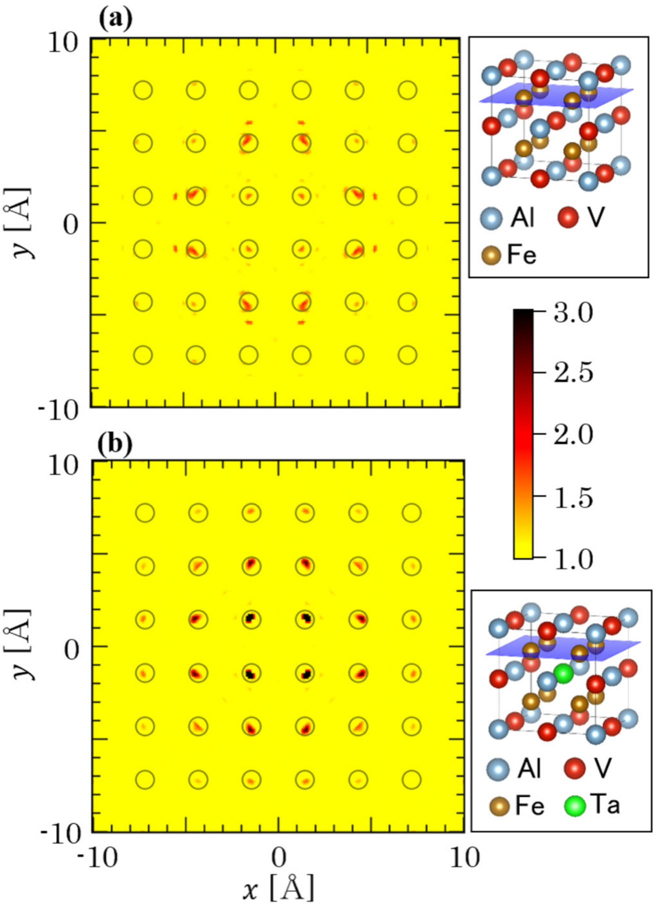

FIG. 6. Reconstructed atomic images of Fe plane around (a) V and (b) Ta. Circles indicate the expected positions of Fe atoms.

acoustic and optical phonons are enhanced in the vicinity of strong and weak Bragg reflections, respectively [50]. This effect is clearly reflected in the obtained IXS spectra. The spectra in Figs. 7(a) and 7(b) are dominated by the acoustic phonons indicated by arrows. On the other hand, optical phonons indicated by bars are detectable in Figs. 7(c) and 7(d) at around 30 and 45 meV, while the acoustic phonons are strongly suppressed.

The spectra shown in Figs. 7(a) and 7(c) contain two propagating modes, which can be attributed to the longitudinal and transverse modes. These results are caused by the location of the analyzer crystals installed at the IXS spectrometer of BL35XU at the SPring-8. The location of the analyzer crystals slightly deviated from the high-symmetry direction even when the sample orientation was well aligned. Consequently, the spectrometer detects the transverse (longitudinal) modes because of polarization effects even in the geometry for the measurement in the longitudinal (transverse) direction. However, if the deviations in the measured Q positions are smaller than the magnitude of the propagation vectors from the Γ points, one can reasonably approximate the direction of the propagation vectors to the high-symmetry direction. Thus, these deviations do not significantly affect the discussion of the phonon dispersion relations in the present case.

The features described above are also observed for the IXS spectra of $Fe_2(V_{0.95}Ta_{0.05})Al$ [Figs. 7(e)–7(h)], and their overall shapes are similar to those of Fe_2VAl. However, a remarkable difference from the spectra of Fe_2VAl can be observed, i.e., a very broad peak located at around 17 meV. It is reasonable to suppose that this additional mode is a Ta-doping effect.

To derive the phonon dispersions, the fitting to the IXS spectra was done based on the damped harmonic oscillator (DHO) model [51]. The solid curves are the results of the fitting. In Figs. 7(e)–7(h), the DHO component of the broad feature at around 17 meV is indicated by the curves filled with blue shading.

IV. DISCUSSION

A. Local structure

In general, the large values of the rms displacement and weak atomic image intensities observed in XAFS and XFH, respectively, are caused by lattice distortions and thermal vibrations. In the present case, it is inconceivable that the lattice distortion around the matrix element of V is larger than that around the doped element of Ta. Although doped Ta atoms can induce lattice distortions around V considering the concentration of the dopant, the XAFS experiment shows that Ta doping has only a little influence on the height of the first peak in $|F(r)|$ or the values of σ_i around V. Furthermore, the lattice distortions are unlikely to cause the difference in the atomic images around V and Ta over the wide range of more than 10 Å (Fig. 6) since they usually affect the atomic images of only first- or second-nearest neighbors. Therefore, the difference in the local structures around V and Ta can be attributed to the difference in their thermal vibrations.

The XAFS and XFH results indicate that such a thermal vibration is characterized by a much stronger positional correlation between Ta and Fe than between V and Fe. This feature is quantified by the rms displacements shown in Table I. Similarly, XFH can provide quantitative information about this feature based on the difference in the atomic image intensities around Ta from those around V.

The Fe atomic image intensities obtained with XFH are plotted in Fig. 8 as a function of the distance from V or Ta r. Here, the intensity is normalized by that of first-nearest Fe atom around Ta. To quantify the difference in the Fe intensities around V and Ta, the function a/r (a is a fitting parameter) was fitted to the data points based on the fact that the holographic oscillation is inversely proportional to r [19,20]. The solid and dashed curves are the results of the fitting. The ratio of the parameter a for the Fe intensities around V to those around Ta is evaluated to be 0.63 ± 0.10.

To evaluate the magnitude of the positional fluctuations between Fe and the emitter (Ta or V), a calculation of holograms and atomic images was done based on the atomic coordinates taking these fluctuations into account. The positional fluctuations are expressed as a three-dimensional Gaussian, $G(\boldsymbol{x}) = (1/\sqrt{2\pi}s)\exp[-(\boldsymbol{x}-\boldsymbol{x}_0)^2/2s^2]$, where $\boldsymbol{x}_0$ is an ideal relative position between Fe and the emitter. The magnitude of the positional fluctuation can be evaluated from the half width at half maximum δ of the Gaussian, given by $\delta = \sqrt{2\ln 2}s$. The calculation was carried out using 3D-AIR-IMAGE [52], the software for analyzing and calculating x-ray fluorescence and

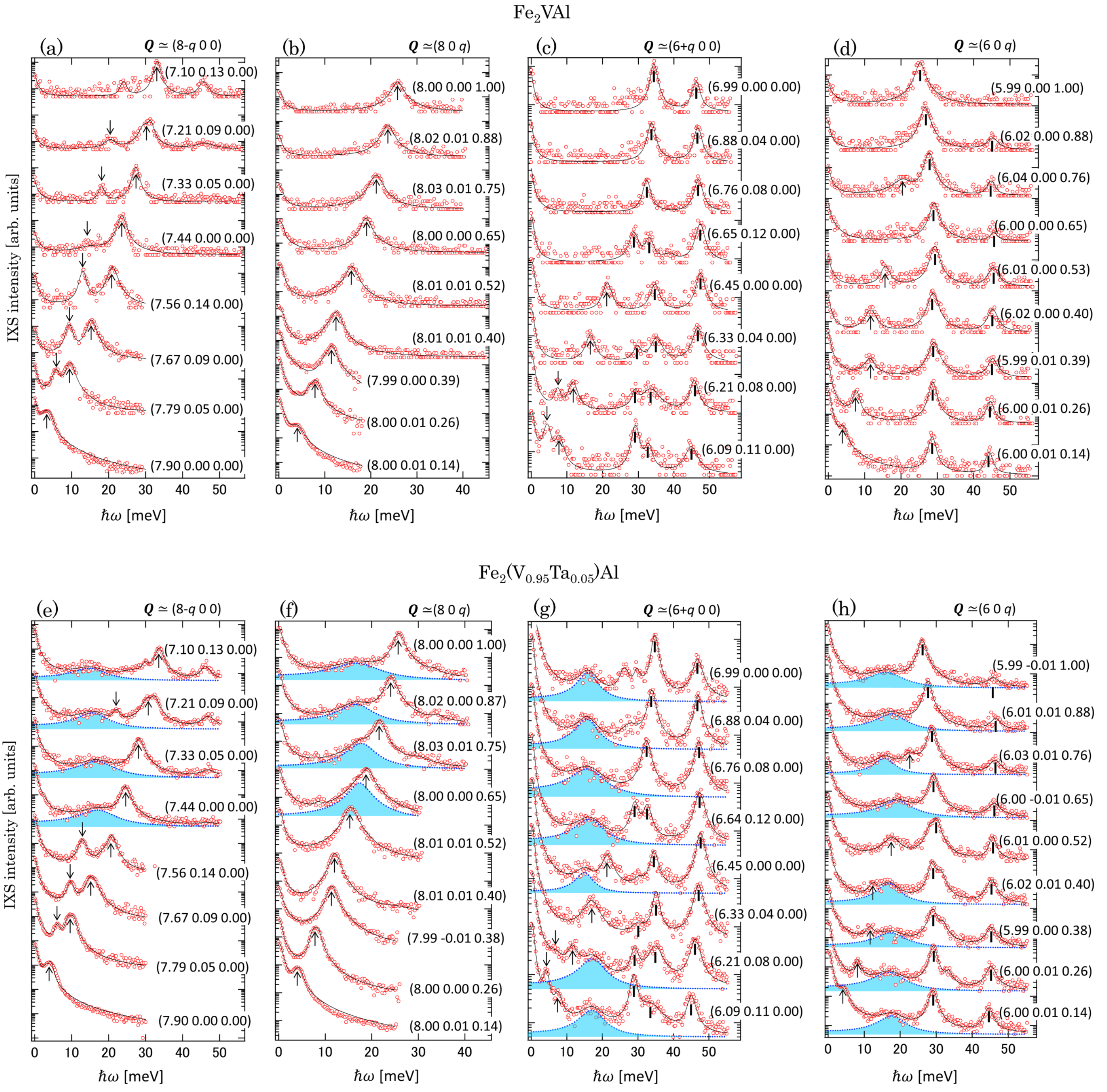

FIG. 7. (a)–(d) The IXS spectra of $\mathrm{Fe_2VAl}$ measured in the geometry to detect LA, TA, LO, and TO modes, respectively. (e)–(h) The corresponding IXS spectra of $\mathrm{Fe_2(V_{0.95}Ta_{0.05})Al}$. Solid curves are the results of the fitting using the DHO model.

photoelectron holograms. Figure 9(a) shows the calculated intensity of the first-nearest-neighbor (NN) Fe image as a function of δ. Figure 9(b) illustrates the positional fluctuations expressed by the Gaussian, which was used in the calculation. We observe that Fe intensity monotonically decreases with increasing δ in a systematic manner, and thus, the difference in the V-Fe and Ta-Fe positional correlations can be evaluated from the experimentally obtained Fe atomic image intensities.

According to the Rietveld analysis of powder neutron diffraction measurements for $\mathrm{Fe_2VAl}$ [43], atomic displacement parameters of V and Fe (denoted as B_{V} and B_{Fe}) are reported as $B_{\mathrm{V}} = 0.8(1)$ Å^2 and $B_{\mathrm{Fe}} = 0.37$ Å^2. From these values, the magnitude of the positional fluctuation between V and Fe $\delta_{\text{V–Fe}}$ is estimated to be $\sqrt{B_{\mathrm{V}}/8\pi^2 + B_{\mathrm{Fe}}/8\pi^2} = 0.12$ Å if V and Fe atoms randomly oscillate around the lattice points. On the other hand, if we assume an antiphase movement of V and Fe as described in Ref. [36], $\delta_{\text{Fe–V}}$ is estimated to be $\sqrt{B_{\mathrm{V}}/8\pi^2} + \sqrt{B_{\mathrm{Fe}}/8\pi^2} = 0.17$ Å, which can be regarded as the maximum value of $\delta_{\text{Fe–V}}$. When $\delta_{\text{V–Fe}}$ takes this maximum value of 0.17 Å, the normalized first-NN Fe image intensity is 0.55 as displayed in Fig. 9(a). Since the ratio of the Fe atomic image intensity around V to that around Ta is 0.63, the Fe image intensity around Ta is estimated to be $0.55/0.63 = 0.87$. Thus, it is indicated that the value of $\delta_{\text{Ta–Fe}}$ is less than 0.07 Å, as shown in Fig. 9(a), which

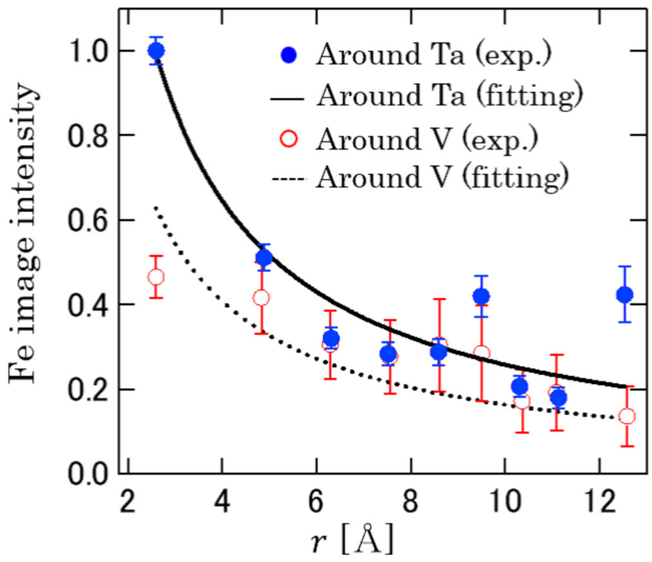

FIG. 8. Intensities of Fe atomic images around V and Ta as a function of the distance from the emitter r.

confirms a much more robust correlation between Ta and Fe than between V and Fe.

B. Phonon dispersions

Figures 10(a) and 10(b) show phonon dispersions of Fe_2VAl and $Fe_2(V_{0.95}Ta_{0.05})Al$ obtained by the fitting. The solid curves are the results of the calculation for Fe_2VAl obtained by using the PHASE code [53], a program package performing first-principles calculations based on density functional theory. Here, the generalized gradient approximation was used as the exchange-correlation term [54]. The experimental results of both Fe_2VAl and $Fe_2(V_{0.95}Ta_{0.05})Al$ agree with the calculated results, except for the modes observed at around 17 meV in $Fe_2(V_{0.95}Ta_{0.05})Al$, which is indicated in the shaded area in Fig. 10(b). These modes correspond to the broad peaks shown in Figs. 7(e)–7(h). These experimental facts indicate that the phonon dispersion relations are insensitive to Ta doping except for the additional modes observed at around 17 meV.

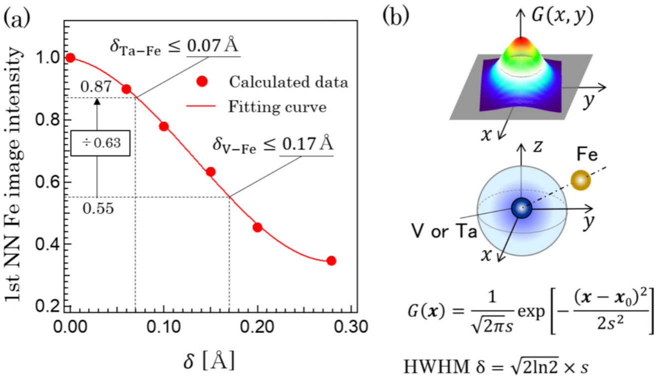

FIG. 9. Calculated intensity of the first-nearest-neighbor (NN) Fe image as a function of the magnitude of the positional fluctuation δ. (b) Illustration of the positional fluctuation used in the calculation.

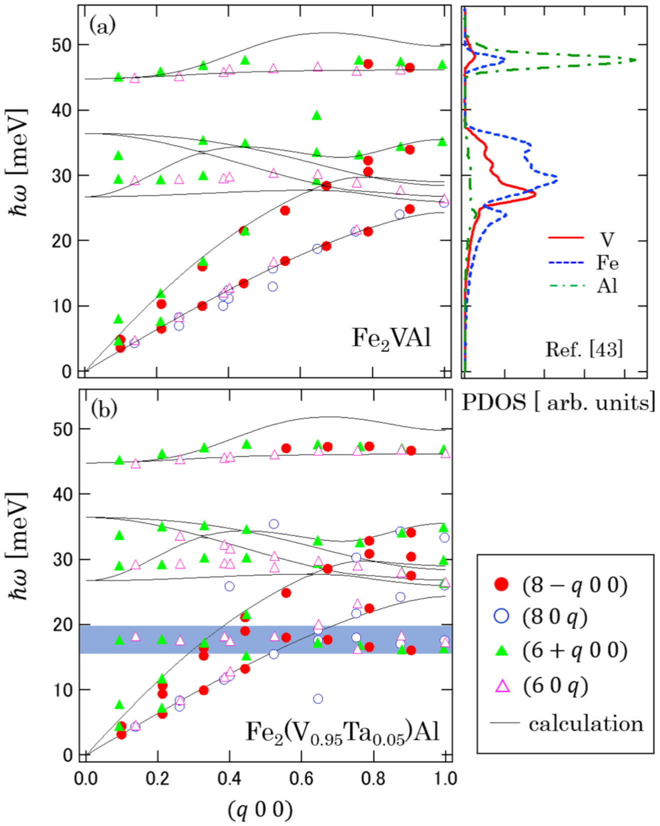

FIG. 10. Phonon dispersions of (a) Fe_2VAl and (b) $Fe_2(V_{0.95}Ta_{0.05})Al$. The solid curves are the result of the calculation [53] for Fe_2VAl. The partial density of states (PDOS) taken from Ref. [43] is also shown in the top right.

The vibration of an atom of different mass in a crystal has been investigated for a long time [11,55,56]. According to Refs. [11,55], the addition of a heavy atom to a crystal can cause the so-called resonant modes. The resonant mode has been observed in Au-doped Cu [57], W-doped Cr [58], and, recently, Os- or Ir-doped FeSi [9] using the INS technique. In the case of Os-doped FeSi [9], for example, the excitation energy of the Os resonant mode can be explained by the mass ratio of the doped element to the host element. The Os resonant mode is observed at about 17 meV, whereas the Fe optical mode is observed in the energy range from 28 to 35 meV. The ratio of the phonon energy of the Os resonant mode to that of the Fe optical mode agrees well with the value calculated from the square root of the ratio of the Fe mass to the Os mass. Note that the energies of vibrational modes are proportional to the inverse of the square root of the atomic mass.

The above idea of the resonant mode is applicable to the interpretation of the additional modes observed in the present work. The right side of Fig. 10(a) is the PDOS of Fe_2VAl taken from Ref. [43]. The optical mode at around 45 meV is mainly attributed to the vibration of Al, while that in the range of 30–35 meV is due to the vibration of Fe and V. In $Fe_2(V_{0.95}Ta_{0.05})Al$, V is substituted by Ta, and thus, the vibrational mode of Ta should appear at around $\sqrt{M_V/M_{Ta}}$ times the vibrational energy of V. From the value of $\sqrt{M_V/M_{Ta}} = 0.53$ and the vibrational energy of V, 30–35 meV, the vibrational energy of Ta can be estimated to be 15.9–18.6 meV, which is in good agreement with the energy of the additional mode. Therefore, the additional mode can be attributed to the vibration of Ta.

C. Effect of the additional mode on κ_{ph}

In order to discuss the effect of the additional mode on κ_{ph}, it is helpful to refer to the isotopic effect on the thermal conductivity of the diamond [59], where the reduction in the thermal conductivity was observed with increasing concentration of the ^{13}C isotope. Since the electronic structure is not affected by the isotopic substitution, the isotopic effect on the thermal conductivity is caused by the difference in the masses between ^{12}C and ^{13}C. In other words, the isotopic substitution does not change the force constant working on the C atoms. The difference in the masses results in the difference in the vibrational frequencies or the kinetic energies between ^{12}C and ^{13}C, which disturbs the coherency of the phonons, and consequently, κ_{ph} should become lower. This situation is similar to the present case of Ta-doped Fe_2VAl since the excitation energy of the additional mode can be sensibly evaluated only from the mass difference between V and Ta, as discussed above. This indicates that the force constant working on Ta atoms is equal to that on V within the experimental error. The observation of the additional modes clearly shows that the vibrational frequency of Ta is different from V, which implies that thermal insulation in $Fe_2(V_{0.95}Ta_{0.05})Al$ is caused by the disturbance of the coherency of the phonons in Fe_2VAl.

The linewidth of the additional modes is broader than the optical modes observed in the present work, which also disturbs the coherency of phonons and thus will enhance the thermal insulation. The broad feature of the dopant mode has been observed in previous studies on the resonant mode, such as the INS study [9] and the theoretical study based on the linear chain model [56]. Therefore, the broad linewidth of the additional mode can be attributed to the inherent character of the resonant mode. Moreover, if the distribution of Ta atoms is not completely homogeneous, the linewidth can become broader because the potential at each Ta position depends on whether Ta atoms are isolated or aggregated. Although electron-phonon coupling and phonon-phonon interaction can also cause the line broadening, these effects are not expected to be significant. This is because the excitation energy of the additional mode can be explained without considering the difference of the force constant working on Ta from that working on V, which indicates that the electron-phonon coupling is not strong. Also, evident line broadening of the acoustic modes is not observed in the present results, suggesting a weak phonon-phonon interaction.

The local structural analysis based on the EXAFS and XFH techniques showed that Ta-Fe correlation is much stronger than the V-Fe correlation, which can also cause the disturbance of the phonon coherency. This difference in the positional correlation can be attributed to the character of the Ta additional modes. The real-space feature of the dopant vibration was mentioned in Refs. [58,60] and also was discussed on the basis of a simple linear chain model [56]. According to these studies, the resonant mode is characterized by a large amplitude of vibration at the dopant and the gradual decay into a host mode at large distances. This is in contrast to the case of a light dopant, in which the vibration at the dopant with a large amplitude rapidly decays in space, resulting in a considerably smaller amplitude of the vibration of neighboring atoms. The character of the resonant mode indicates that the thermal vibration of the heavy dopant is not independent of that of the surrounding atoms, unlike the usual Einstein-like thermal vibration of host atoms. The stronger Fe atomic images around Ta [Fig. 6(b)] and the smaller rms displacement of the Ta-Fe correlation [Fig. 4(b) and Table I] can be explained by this feature of the resonant mode.

V. CONCLUSION

XAFS, XFH, and IXS experiments were performed on $Fe_2(V_{0.95}Ta_{0.05})Al$ to investigate the local structure and the atomic dynamics of Ta. The combination of these techniques revealed the distinct features of the dopant dynamics, which are clearly different from the dynamics of the host element, that is, a much stronger Ta-Fe correlation than V-Fe correlation, lower frequency of the Ta vibration, and a broader linewidth of the Ta additional modes. These features are in accordance with the character of the resonant mode and disturb the coherency of phonons, which should contribute to the improvement of the thermal insulation.

ACKNOWLEDGMENTS

The authors are grateful for Prof. S. Ohara for kindly allowing us to use the furnace for a single-crystal growth. This work was partially supported by a Grant-in-Aid for Young Scientists (B) (Grant No. 17K14801), Scientific Research on Innovative Areas "3D active Site Science" (Grants No. 26105006 and No. 26105013) and "Materials science on mille-feuille structure" (Grant No. 19H05126), Scientific Research (A) (Grant No. 19H00655), and Scientific Research (B) (Grant No. 16H03849) from the Japan Society for the Promotion of Science. This work was also supported by the Naito Science & Engineering Foundation and the Mazda Foundation. The XAFS, XFH, and IXS experiments were performed at BL01B1, BL13XU, and BL35XU of the SPring-8 with the approval of the Japan Synchrotron Radiation Research Institute (JASRI) (Proposals No. 2016A1097, No. 2016A1348, No. 2017A0910, No. 2017A1492, No. 2017B1531, No. 2018A1400, No. 2018A1461, No. 2018A1763, and No. 2018B1540). The XFH experiments were also performed under the approval of the Photon Factory Program Advisory Committee (Proposal No. 2016G592).

---

[1] P. G. Klemens, Proc. Phys. Soc., London, Sect. A **68**, 1113 (1955).

[2] J. M. Ziman, *Electrons and Phonons* (Oxford, Clarendon, 1960).

[3] J. Callaway, Phys. Rev. **113**, 1046 (1959).

[4] W. Li, L. Lindsay, D. A. Broido, D. A. Stewart, and N. Mingo, Phys. Rev. B **86**, 174307 (2012).

[5] Z. Tian, J. Garg, K. Esfarjani, T. Shiga, J. Shiomi, and G. Chen, Phys. Rev. B **85**, 184303 (2012).

[6] J. Shiomi, K. Esfarjani, and G. Chen, Phys. Rev. B **84**, 104302 (2011).

[7] G. S. Nolas, J. L. Cohn, and G. A. Slack, Phys. Rev. B **58**, 164 (1998).

[8] G. S. Nolas, J. L. Cohn, G. A. Slack, and S. B. Schujman, Appl. Phys. Lett. **73**, 178 (1998).

[9] O. Delaire, I. I. Al-Qasir, A. F. May, C. W. Li, B. C. Sales, J. L. Niedziela, J. Ma, M. Matsuda, D. L. Abernathy, and T. Berlijn, Phys. Rev. B **91**, 094307 (2015).

[10] B. C. Sales, O. Delaire, M. A. McGuire, and A. F. May, Phys. Rev. B **83**, 125209 (2011).

[11] P. G. Dawber, R. J. Elliott, and N. Kurti, Proc. R. Soc. London, Ser. A **273**, 222 (1963).

[12] T. M. Gibbons and S. K. Estreicher, Phys. Rev. Lett. **102**, 255502 (2009).

[13] Y. Nishino, M. Kato, S. Asano, K. Soda, M. Hayasaki, and U. Mizutani, Phys. Rev. Lett. **79**, 1909 (1997).

[14] K. Momma and F. Izumi, J. Appl. Crystallogr. **44**, 1272 (2011).

[15] G. J. Snyder and E. S. Toberer, Nat. Mater. **7**, 105 (2008).

[16] Y. Nishino, S. Deguchi, and U. Mizutani, Phys. Rev. B **74**, 115115 (2006).

[17] M. Mikami, Y. Kinemuchi, K. Ozaki, Y. Terazawa, and T. Takeuchi, J. Appl. Phys. **111**, 093710 (2012).

[18] M. Tegze and G. Faigel, Nature (London) **380**, 49 (1996).

[19] K. Hayashi, N. Happo, S. Hosokawa, W. Hu, and T. Matsushita, J. Phys.: Condens. Matter **24**, 093201 (2012).

[20] K. Hayashi and P. Korecki, J. Phys. Soc. Jpn. **87**, 061003 (2018).

[21] T. He, X. Yang, T. Terao, T. Uchiyama, T. Ueno, K. Kobayashi, J. Akimitsu, T. Miyazaki, T. Nishioka, K. Kimura, K. Hayashi, N. Happo, H. Yamaoka, H. Ishii, Y.-F. Liao, H. Ota, H. Goto, and Y. Kubozono, Phys. Rev. B **97**, 104503 (2018).

[22] J. R. Stellhorn, Y. Ideguchi, S. Hosokawa, N. Happo, T. Matsushita, K. Yubuta, M. Suzuki, H. Ishii, Y.-F. Liao, K. Kimura, and K. Hayashi, Surf. Interface Anal. **50**, 790 (2018).

[23] T. Yamamoto, K. Hayashi, N. Happo, S. Hosokawa, and H. Tajiri, Acta Mater. **131**, 534 (2017).

[24] S. Hosokawa, J. R. Stellhorn, T. Matsushita, N. Happo, K. Kimura, K. Hayashi, Y. Ebisu, T. Ozaki, H. Ikemoto, H. Setoyama, T. Okajima, Y. Yoda, H. Ishii, Y.-F. Liao, M. Kitaura, and M. Sasaki, Phys. Rev. B **96**, 214207 (2017).

[25] J. R. Stellhorn, S. Hosokawa, N. Happo, H. Tajiri, T. Matsushita, K.Kaminaga, T. Fukumura, T. Hasegawa, and K. Hayashi, J. Appl. Crystallogr. **50**, 1583 (2017).

[26] A. Sato-Tomita, N. Shibayama, N. Happo, K. Kimura, T. Okabe, T. Matsushita, S.-Y. Park, Y. C. Sasaki, and K. Hayashi, Rev. Sci. Instrum. **87**, 063707 (2016).

[27] Y. Wakabayashi, D. Nakajima, Y. Ishiguro, K. Kimura, T. Kimura, S. Tsutsui, A. Q. R. Baron, K. Hayashi, N. Happo, S. Hosokawa, K. Ohwada, and S. Nakatsuji, Phys. Rev B **93**, 245117 (2016).

[28] Y. Ideguchi, K. Kamimura, K. Kimura, S. Hosokawa, N. Happo, K. Hayashi, Y. Ebisu, T. Ozaki, J. R. Stellhorn, M. Suzuki, H. Okazaki, A. Yamashita, and Y. Takano, Z. Phys. Chem. **230**, 489 (2016).

[29] W. Hu, K. Hayashi, T. Fukumura, K. Akagi, M. Tsukada, N. Happo, S. Hosokawa, K. Ohwada, M. Takahasi, M. Suzuki, and M. Kawasaki, Appl. Phys. Lett. **106**, 222403 (2015).

[30] K. Kimura, K. Hayashi, L. V. Yashina, N. Happo, T. Nishioka, Y. Yamamoto, Y. Ebisu, T. Ozaki, S. Hosokawa, T. Matsushita, and H. Tajiri, Surf. Interface Anal. **51**, 51 (2019).

[31] T. Nishioka, Y. Yamamoto, K. Kimura, K. Hagihara, H. Izuno, N. Happo, S. Hosokawa, E. Abe, M. Suzuki, T. Matsushita, and K. Hayashi, Materialia **3**, 256 (2018).

[32] K. Kimura, K. Hayashi, K. Hagihara, H. Izuno, N. Happo, S. Hosokawa, M. Suzuki, and H. Tajiri, Mater. Trans. **58**, 539 (2017).

[33] K. Hayashi, N. Uchitomi, K. Yamagami, A. Suzuki, H. Yoshizawa, J. T. Asubar, N. Happo, and S. Hosokawa, J. Appl. Phys. **119**, 125703 (2016).

[34] W. Hu, K. Hayashi, K. Ohwada, J. Chen, N. Happo, S. Hosokawa, M. Takahasi, A. A. Bokov, and Z.-G. Ye, Phys. Rev. B **89**, 140103(R) (2014).

[35] N. Happo, M. Fujiwara, K. Tanaka, S. Hosokawa, and K. Hayashi, J. Electron Spectrosc. **181**, 154 (2010).

[36] S. Hosokawa, N. Happo, and K. Hayashi, Phys. Rev. B **80**, 134123 (2009).

[37] Z. Tian, M. Li, Z. Ren, H. Ma, A. Alatas, S. D. Wilson, and J. Li, J. Phys.: Condens. Matter **27**, 375403 (2015).

[38] S. Tsutsui, H. Uchiyama, J. P. Sutter, A. Q. R. Baron, M. Mizumaki, N. Kawamura, T. Uruga, H. Sugawara, J.-i. Yamaura, A. Ochiai, T. Hasegawa, N. Ogita, M. Udagawa, and H. Sato, Phys. Rev. B **86**, 195115 (2012).

[39] S. Tsutsui, H. Kobayashi, D. Ishikawa, J. P. Sutter, A. Q. R. Baron, T. Hasegawa, N. Ogita, M. Udagawa, Y. Yoda, H. Onodera, D. Kikuchi, H. Sugawara, C. Sekine, I. Shirotani, and H. Sato, J. Phys. Soc. Jpn. **77**, 033601 (2008).

[40] M. Rotter, P. Rogl, A. Grytsiv, W. Wolf, M. Krisch, and A. Mirone, Phys. Rev. B **77**, 144301 (2008).

[41] D. J. Voneshen, K. Refson, E. Borissenko, M. Krisch, A. Bosak, A. Piovano, E. Cemal, M. Enderle, M. J. Gutmann, M. Hoesch, M. Roger, L. Gannon, A. T. Boothroyd, S. Uthayakumar, D. G. Porter, and J. P. Goff, Nat. Mater. **12**, 1028 (2013).

[42] V. Kanchana, G. Vaitheeswaran, Y. Ma, Y. Xie, A. Svane, and O. Eriksson, Phys. Rev. B **80**, 125108 (2009).

[43] S. Maier, S. Denis, S. Adam, J.-C. Crivello, J.-M. Joubert, and E. Alleno, Acta Mater. **121**, 126 (2016).

[44] S. S. Shastri and S. K. Pandy, Comput. Mater. Sci. **155**, 282 (2018).

[45] K. Renard, A. Mori, Y. Yamada, S. Tanaka, H. Miyazaki, and Y. Nishino, J. Appl. Phys. **115**, 033707 (2014).

[46] A. L. Ankudinov, B. Ravel, J. J. Rehr, and S. D. Conradson, Phys. Rev. B **58**, 7565 (1998).

[47] D. T. Dul, K. M. Dabrowski, and P. Korecki, Euro Phys. Lett. **104**, 66001 (2013).

[48] J. J. Barton, Phys. Rev. Lett. **67**, 3106 (1991).

[49] A. Q. R. Baron, Y. Tanaka, S. Goto, K. Takeshita, T. Matsushita, and T. Ishikawa, J. Phys. Chem. Solids **61**, 461 (2000).

[50] A. Q. R. Baron, J. Spectrosc. Soc. Jpn. **58**, 205 (2009) [arXiv:0910.5764].

[51] B. Fåk and B. Dorner, Phys. B (Amsterdam, Neth.) **234–236**, 1107 (1997).

[52] 3D-AIR-IMAGE, https://osdn.jp/projects/tmcoca/releases/p14436.

[53] See the website of the PHASE project of the National Institute for Materials Science, https://azuma.nims.go.jp.

[54] J. P. Perdew, K. Burke, and M. Ernzerhof, Phys. Rev. Lett. **77**, 3865 (1996).

[55] R. J. Elliott and D. W. Taylor, Proc. R. Soc. London, Ser. A **296**, 161 (1967).

[56] A. S. Baker, Jr., and A. J. Sievers, Rev. Mod. Phys. **47**, S1 (1975).

[57] E. C. Svensson and B. N. Brockhouse, Phys. Rev. Lett. **18**, 858 (1967).

[58] H. B. Moller and A. R. Mackintosh, Phys. Rev. Lett. **15**, 623 (1965).

[59] J. R. Olson, R. O. Pohl, J. W. Vandersande, A. Zoltan, T. R. Anthony, and W. F. Banholzer, Phys. Rev. B **47**, 14850 (1993).

[60] *Elementary Excitations in Solids*, edited by A. A. Maradudin and G. F. Nardelli (Plenum, New York, 1969), p. 35.